AGU PUBLICATIONS

JGR

Journal of Geophysical Research: Solid Earth

RESEARCH ARTICLE
10.1002/2015JB012227

Key Points:
- Multiparametric approach is effective to investigate plumbing system pressurization-depressurization
- It was shown how shallow explosion can modify the volcano conditions down to several kilometers below sea level
- It was shown how depressurization quickly propagated downward triggering uprises of magma/gas

Supporting Information:
- Figure S1

Correspondence to:
A. Cannata,
andrea.cannata@ingv.it

Citation:
Cannata, A., G. Spedalieri, B. Behncke, F. Cannavò, G. Di Grazia, S. Gambino, S. Gresta, S. Gurrieri, M. Liuzzo, and M. Palano (2015), Pressurization and depressurization phases inside the plumbing system of Mount Etna volcano: Evidence from a multiparametric approach, *J. Geophys. Res. Solid Earth*, *120*, 5965–5982, doi:10.1002/2015JB012227.

Received 20 MAY 2015
Accepted 7 AUG 2015
Accepted article online 13 AUG 2015
Published online 11 SEP 2015

Pressurization and depressurization phases inside the plumbing system of Mount Etna volcano: Evidence from a multiparametric approach

Andrea Cannata[1], Giancarlo Spedalieri[2], Boris Behncke[1], Flavio Cannavò[1], Giuseppe Di Grazia[1], Salvatore Gambino[1], Stefano Gresta[2], Sergio Gurrieri[3], Marco Liuzzo[3], and Mimmo Palano[1]

[1]Istituto Nazionale di Geofisica e Vulcanologia, Osservatorio Etneo, Sezione di Catania, Catania, Italy, [2]Dipartimento di Scienze Biologiche, Geologiche e Ambientali, Sezione Scienze della Terra, Università di Catania, Catania, Italy, [3]Istituto Nazionale di Geofisica e Vulcanologia, Sezione di Palermo, Palermo, Italy

Abstract During 2013 Mount Etna volcano experienced intense eruptive activity at the summit craters, foremost at the New Southeast Crater and to a minor degree at the Voragine and Bocca Nuova (BN), which took place in two cycles, February–April and September–December. In this work, we mainly focus on the period between these cycles, applying a multiparametric approach. The period from the end of April to 5 September showed a gradual increase in the amplitude of long-period (LP) events and volcanic tremor, a slight inflation testified by both tilt and GPS data, and a CO_2 flux increase. Such variations were interpreted as due to a gradual pressurization of the plumbing system, from the shallowest part, where LP and volcanic tremor are located, down to about 3–9 km below sea level, pressure source depths obtained by both geodetic and CO_2 data. On 5 September, at the same time as a large explosion at BN, we observed an instantaneous variation of the aforementioned signals (decrease in amplitude of LP events and volcanic tremor, slight deflation, and CO_2 flux decrease) and the activation of a new infrasonic source located at BN. In the light of it, the BN explosion probably caused the instantaneous end of the pressurization, and the opening of a new vent at BN, that has become a new steady source of infrasonic events. This apparently slight change in the plumbing system also led to the gradual resumption of activity at the New Southeast Crater, culminating with the second lava fountain cycle of 2013.

1. Introduction

Eruptions are preceded by magma movements and pressure increases, involving the plumbing systems, especially in closed volcanic systems [e.g., *Chaussard et al*., 2013]. Such phenomena can produce elastic wave radiation, due to both rock failure (volcano-tectonic earthquakes) and fluid dynamics (volcanic tremor and long-period seismicity), ground deformation, and geochemical variations [e.g., *Scarpa and Gasparini*, 1996; *Kilburn and Voight*, 1998]. Each monitoring parameter, taken individually, has advantages and drawbacks, and for this reason cannot be considered totally reliable for volcano monitoring purposes. Hence, the more methods that can be used at one time, the better will be the chances of detecting precursory variations [e.g., *McNutt et al*., 2000]. The multiparametric approach is useful not only for monitoring/surveillance purposes but also for investigating the volcano dynamics and reconstructing the plumbing system. For instance, *Rivet et al*. [2014] revealed inflation-deflation cycles at Piton de la Fournaise volcano by seismic velocity change observations and GPS measurements. *Takeo et al*. [2006] reconstructed the magma supply path beneath Mount Asama volcano using dense seismic and geodetic networks.

The summit area of Mount Etna volcano is characterized by five summit craters: Southeast Crater (hereafter referred to as SEC), New Southeast Crater (NSEC), Bocca Nuova (BN), Voragine (VOR), and Northeast Crater (NEC) (see Figure 1a). From 2011 to 2015, Etna showed an intense activity, with tens of lava fountaining episodes, effusive and Strombolian eruptions from some of these craters. Moreover, a subterminal eruption took place in the summer of 2014. During the last 10 years, Etna was also characterized by gradual and important improvements of the monitoring systems, involving seismic, geodetic, infrasonic, video camera, and geochemical networks [e.g., *Patanè et al*., 2013]. Both intense eruptive activity and effective monitoring systems have made Etna the best volcano to apply a multiparametric approach aimed at investigating the volcano dynamics. For these reasons, during the last years the number of multidisciplinary studies on Mount Etna has been increasing. Some of these studies focus on a single lava fountain episode [e.g., *Bonaccorso et al*., 2011]; others take into account longer time intervals [e.g., *Patanè et al*., 2013].

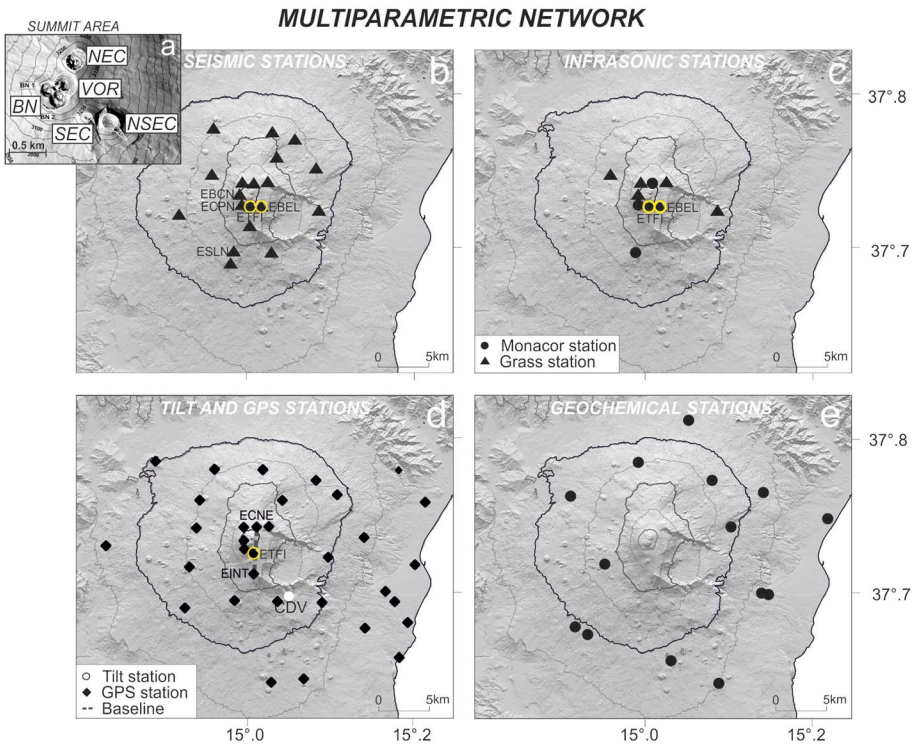

Figure 1. Multiparametric network. (a) Digital elevation model of the summit area of Mount Etna with the summit craters (Bocca Nuova: BN; Voragine: VOR; Northeast Crater: NEC; Southeast Crater: SEC; New Southeast Crater: NSEC). (b) Digital elevation model of Etna with the location of the seismic stations used to analyze the seismo-volcanic signals. (c) Digital elevation model of Etna with the location of the infrasonic stations. (d) Digital elevation model of Etna with the location of the GPS stations (black diamonds), GPS baseline (ECNE-EINT, dashed line), and the tilt station (CDV, white circle) used in this work. (e) Digital elevation model of Etna with the location of the geochemical stations measuring CO_2 flux (one station, located south of the lower figure boundary, is missing in the plot). The yellow circles in Figures 1b–1d indicate the stations destroyed during the paroxysmal episodes of 28 February and 11 November 2013 (EBEL and ETFI, respectively).

In this paper, we study Etna's dynamics during January–December 2013, characterized by a first lava fountain cycle in February–April, a quiescent period from May to September, and a second eruptive cycle from September to December. In particular, we will focus on the quiescent phase by applying a multiparametric approach, which consists of combining seismic (volcanic tremor and long-period events), infrasonic, geodetic (GPS and tilt), volcanological, and geochemical information. This multiparametric approach, involving five different permanent networks (each of one composed of many sensors), proved quite effective to reconstruct the pressurization and depressurization phenomena taking place within the volcano plumbing system at different depths, as well as to obtain insights into its geometry.

2. Volcanic Framework

From the end of the 2008–2009 flank eruption (in July 2009) until the end of 2010, Etna showed only minor explosive activity that involved SEC (Figure 1a) and in particular a pit crater that had formed on the eastern flank of the SEC cone in May 2007 [*Behncke et al*., 2014], BN, and NEC [e.g., *Andronico et al*., 2013; *Patanè et al*., 2013]. The first days of 2011 showed an intensification of explosive activity, with Strombolian activity at the pit crater of the SEC cone culminating in a paroxysmal episode at the same crater that took place on 12 January [*Patanè et al*., 2013]. This was just the first of 25 episodes, which occurred from January 2011 to April 2012 leading to the creation of the new cone of NSEC (Figure 1a) [*Behncke et al*., 2014]. As reported by *Behncke et al*. [2014] and *Viccaro et al*. [2014], all these episodes showed a similar succession of different phases: (i) a reactivation phase with minor explosive activity, (ii) a Strombolian phase often accompanied by lava emission, (iii) a lava fountaining and rapid lava flow emission phase representing the climax of the eruption, and (iv) a waning phase with lava fountaining being gradually replaced by mild and diminishing

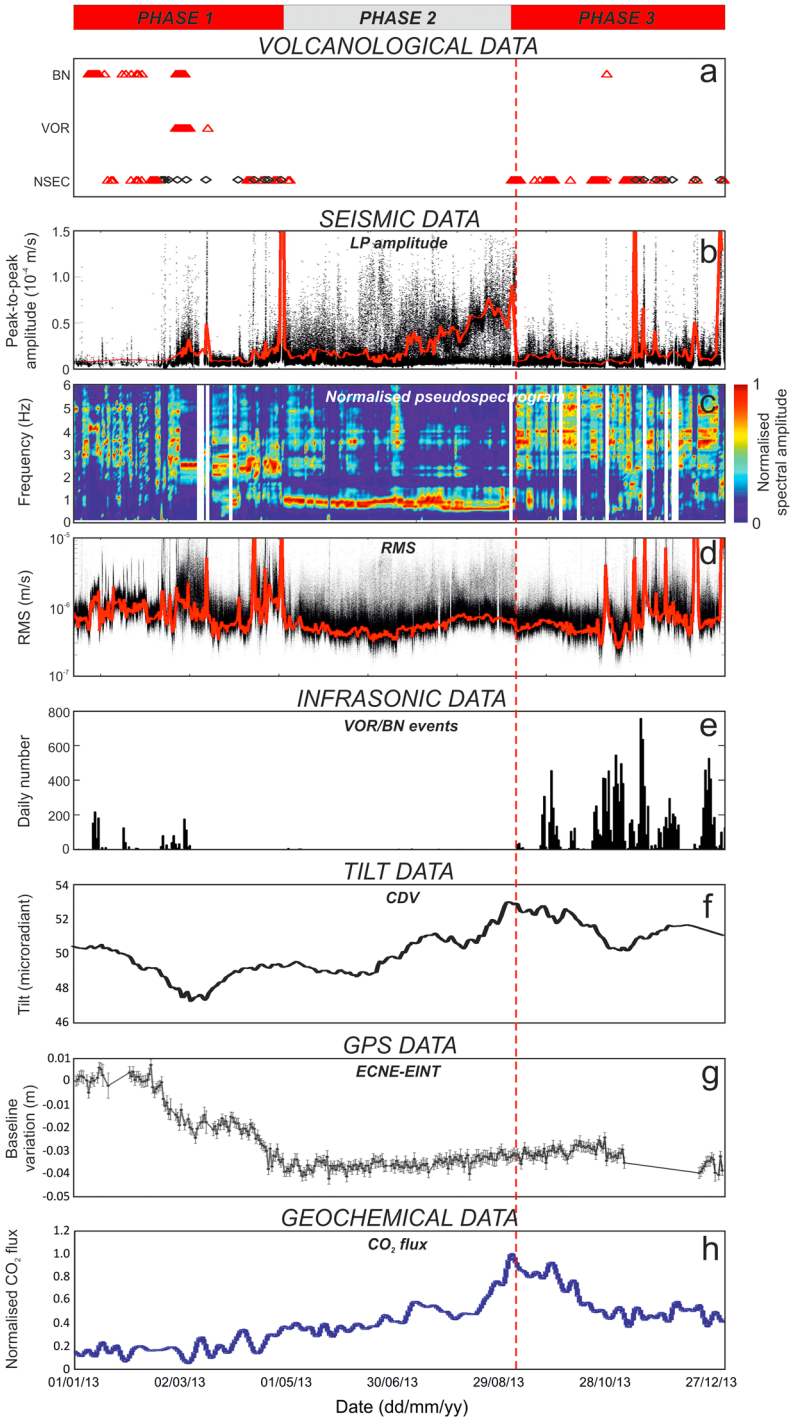

Figure 2. Plot with the main multiparametric data obtained at Mount Etna during 2013. The vertical dashed red line indicates the occurrence time of the explosion at BN, which took place on 5 September 2013 at 15:39. The top red and grey rectangles indicate the time intervals called Phase 1, Phase 2, and Phase 3 (see section 4 for details). (a) Plot summarizing the eruptive activity at BN, VOR, and NSEC (the red triangles and black diamonds indicate Strombolian activity and lava fountaining, respectively). (b) Peak-to-peak amplitude of the LP events detected at Etna (black dots) and relative 75° percentile (red line). (c) Pseudospectrogram of the LP events detected at Etna. (d) RMS amplitude of the vertical component of the seismic signals recorded by ESLN station and filtered in the band 0.5–2.5 Hz (black dots) and relative 25° percentile (red line). (e) Daily number of infrasonic events located in the BN/VOR area. (f) Radial tilt component recorded at CDV station; data are corrected by seasonal oscillations and rain effects. (g) Variation in time of the length of the baseline ECNE-EINT with the 1 sigma associated uncertainties. (h) Total soil CO_2 flux amplitude variations. The locations of all the cited stations are shown in Figure 1.

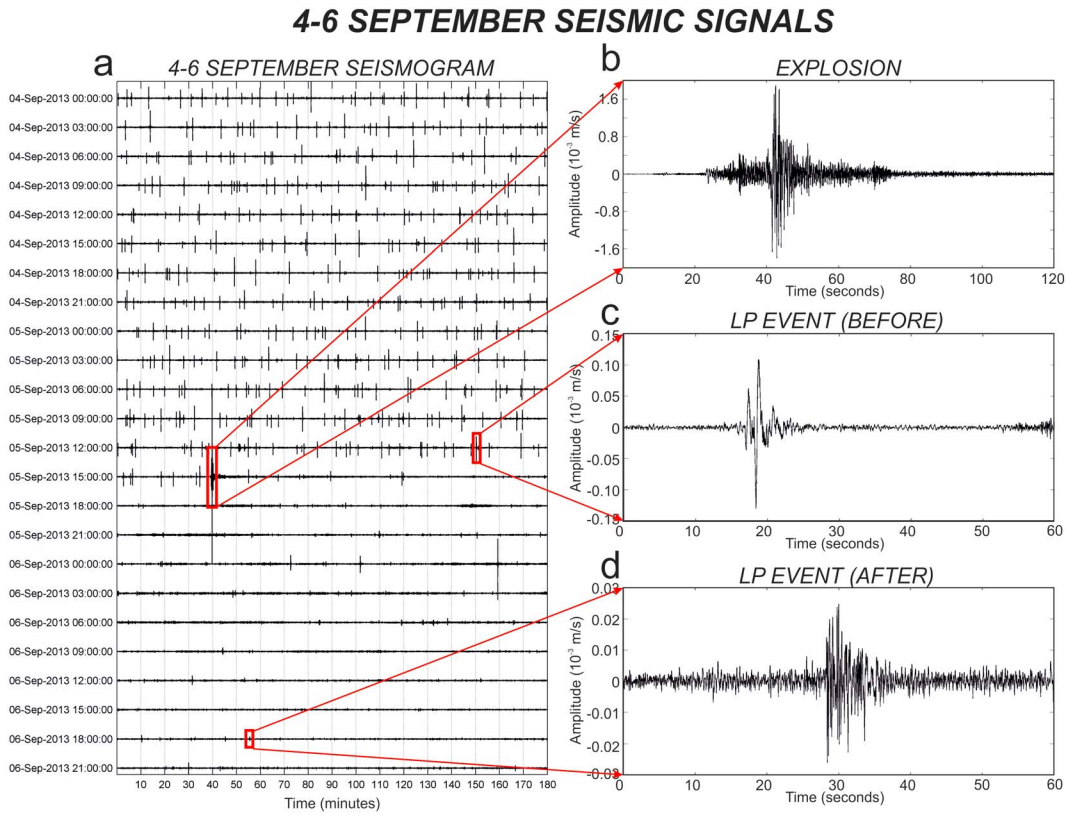

Figure 3. 4–6 September seismic signals. (a) Seismogram of the vertical component of the signal recorded by EBCN station during 4–6 September 2013. (b) Seismic signal recorded by the vertical component of EBCN station during 15:39–15:41 on 5 September 2013, showing the amplitude transient accompanying the explosion at BN. (c) Waveform of the typical LP events, characterized by low-frequency content, recorded at Mount Etna during the period end of April to 5 September 2013 (before the BN explosion time). (d) Waveform of the typical LP events recorded at Mount Etna after the BN explosion time.

Strombolian activity followed by a period of repose. In spite of the very similar eruptive behavior, there were important differences among the episodes mainly regarding the duration of the different phases and in particular of the Strombolian and lava fountaining phases [e.g., *Behncke et al.*, 2014; *Viccaro et al.*, 2014]: as for the former, some events showed slow resumption with prolonged periods of Strombolian activity (up to some days), and others exhibited fast increases of the eruptive intensification reaching the paroxysmal phase after a few hours of Strombolian activity; concerning the latter, the duration ranged from less than 1 h to more than 8 h. During the summer seasons of 2011 and 2012 also the BN was the seat of Strombolian activity and intracrater lava flow emission.

During 2013 the eruptive activity at Etna's summit craters continued rather intensely (see the sketch shown in Figure 2a) [*Spampinato et al.*, 2015]. The first month and a half was characterized by episodic Strombolian activity at the NSEC and BN. In mid-February episodic lava fountaining resumed at the NSEC and took place in two different cycles: February–April and September–December. The former consisted of 13 episodes, the first on 19 February and the last on 27 April. This first cycle was particularly intense, as testified by [*Spampinato et al.*, 2015] (i) the simultaneous explosive activity at the BN and NSEC, joined on 27 February by VOR, which awoke from more than 13 years of quiescence, and (ii) the very high rate of occurrence of lava fountain episodes culminating in four episodes in ~50 h during 19–21 February 2013.

The period from early May to the beginning of September, in contrast, was characterized by the complete absence of eruptive activity; only during the first few days of September, weak Strombolian activity resumed at the NSEC. At 15:39 h UTC (=local time −2), and on 5 September a violent explosion took place at the BN. Although it was not possible to observe this explosion by the surveillance video cameras due to cloud cover, the violence of the explosion was clearly highlighted by its seismic signature (Figures 3a and 3b). Indeed, taking into account the peak-to-peak amplitudes of all the long-period (LP) events detected during

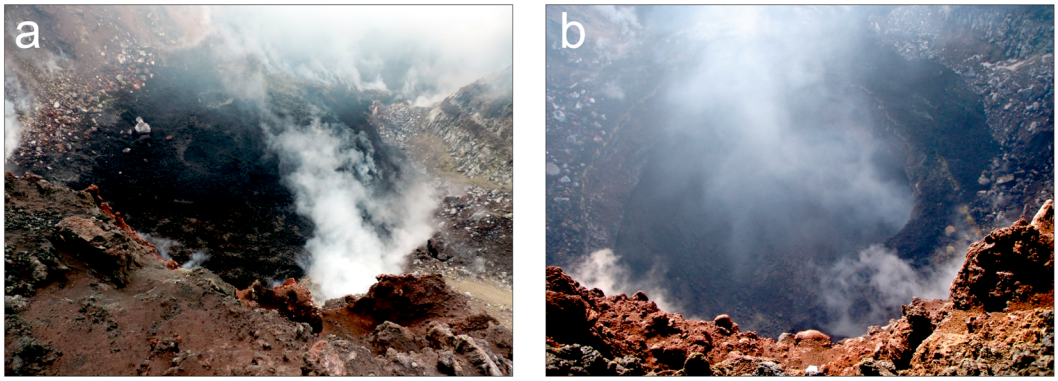

Figure 4. Pictures taken by (a) Boris Behncke on 23 August and by (b) Biagio Ragonese on 7 September 2013, showing the inner part of the BN. Note that the solidified lava flows, which covered the NW sector of the BN before the explosion, resulted to be replaced by a depression after the explosion. Both photographs were taken from approximately the same spot (the western rim of the Bocca Nuova).

2012–2013, the percentile rank of the seismic event accompanying such explosion is higher than 99.9%. The explosion caused an important modification of the BN, as testified by the comparison between the two photos taken on 23 August and 7 September 2013 of the inner part of the crater shown in Figure 4. In particular, the solidified lava flows, which were emitted during 2012 to first months of 2013 and covered the NW sector of the BN before the explosion, were seen to have been replaced by a depression after the explosion. During the hours and days following the BN explosion, explosive activity at NSEC intensified and finally culminated in the paroxysmal episode of 26 October. This was the first paroxysm of the second cycle, which comprised eight lava fountain episodes and ended on 31 December 2013.

3. Data Analysis

In order to reconstruct Etna's dynamics during 2013, different kinds of data were used (see Figure 2): seismic, infrasonic, tilt, GPS, geochemical, and volcanological. In the next sections, all the analyses and results obtained from these data are described.

3.1. Seismic Data

At Mount Etna, the seismic permanent network run by Istituto Nazionale di Geofisica e Vulcanologia (INGV)–Osservatorio Etneo comprises 33 broadband and 12 short-period stations. Analysis of seismo-volcanic signals is performed on the recordings of the 19 stations closest to the summit area. These stations are equipped with broadband (40 s cutoff period), three-component Trillium seismometers (Nanometrics^{TM}) acquiring in real time at a sampling rate of 100 Hz (Figure 1b). It is worth noting that two of these stations (EBEL and ETFI; see yellow circles in Figure 1b) were destroyed during the paroxysmal episodes of 28 February and 11 November 2013, respectively.

We analyzed LP events and volcanic tremor recorded during 2013, as well as the seismic signal accompanying the 5 September BN explosion.

As for the former, we detected more than 200,000 events, whose peak-to-peak amplitudes and spectral features are shown in Figures 2b and 2c, respectively. The peak-to-peak amplitude was obtained from the seismic signal recorded by ECPN station (see Figure 1b), which is the reference station for LP events study at Etna [e.g., *Cannata et al.*, 2009]. Concerning the spectral features, we calculated the normalized pseudospectrogram (examples of the application of pseudospectrograms can be found in *Alparone et al.* [2010] and *Spina et al.* [2014]), allowing to track the evolution of the LP spectral content, as follows: by the FFT algorithm, we calculated one spectrum for each event using a 10 s long window, starting 0.5 s before the onset of the LP event. Next, an averaging process was performed on the amplitude spectra of all the events falling in non-overlapping 1 day windows, sliding through the investigated time interval. Finally, we normalized each spectrum by its maximum value and gathered the normalized averaged spectra as columns in a single matrix arranged in temporal order. This matrix was visualized as a pseudospectrogram with time in the *x* axis, frequency in the *y* axis, and the color scale showing spectral amplitude. From January to mid-February 2013,

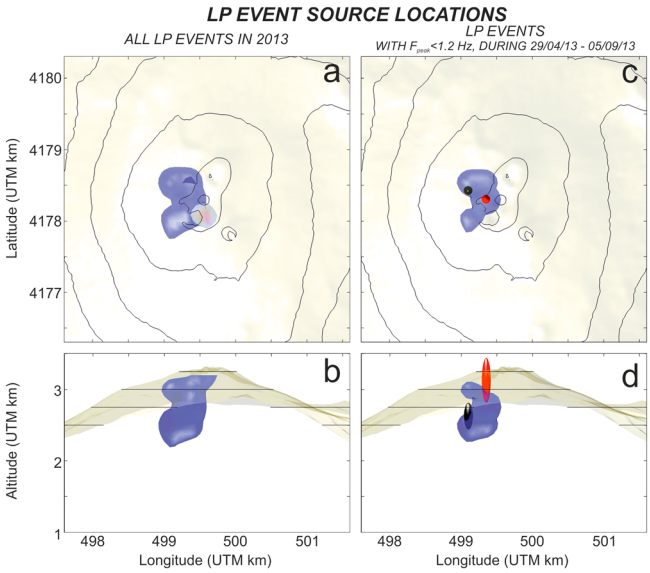

Figure 5. LP event source locations. (a and b) Map and section of Etna with source locations of LP events (blue surface) recorded during 2013. (c and d) Map and section of Etna with source locations of LP events (blue surface) recorded during 28 April 2013 to 5 September 2013 and characterized by low-frequency peaks (<1.2 Hz) and with source location of the initial portion (black ellipsoid) and the maximum amplitude portion (red ellipsoid) of the seismic signal accompanying the BN explosion on 5 September 2013. The blue surface encloses all the grid nodes, used for the grid-search location, with more than 1000 LP event locations. The dimensions of the ellipsoids in Figures 5c and 5d are proportional to the location errors.

LP events were characterized by weak amplitudes (Figure 2b) and relatively broad spectral contents (~2–5 Hz; Figure 2c). During the first cycle of lava fountains of 2013, we observed an increase in the amplitudes of LP events. However, the most important change in terms of both amplitude and spectral content took place successively, during the 28 April to 5 September time interval. Indeed, a gradual amplitude increase occurred, ending on 5 September with a very sharp decrease, at the same time as the explosion at the BN. During the same time interval, we noted an important variation in LP spectral content: most LP events became monochromatic with frequency peaks <1.2 Hz (Figure 2c). Similarly to most of the LP events at Mount Etna, these LP events were not accompanied by acoustic trace. It is also possible to observe a gradual decrease of the frequency peak from ~1.0 Hz to ~0.6 Hz, taking place from May to the end of August. Moreover, this peculiar low-frequency feature sharply ended on 5 September, when the LP event spectral content became again higher and broader (3–6 Hz). The rapidity of the changes of the LP events, which took place at the same time as the 5 September BN explosion, is evident in the seismograms shown in Figure 3: indeed, the disappearance of the "signal spikes" after the BN explosion is due to the strong decrease of LP event amplitude (Figure 3a), while the changes in the LP waveforms are visible in the seismograms in Figure 3c (typical LP event waveform during 28 April to 5 September) and Figure 3d (typical LP event waveform after the explosion).

The LP events were also located by a grid-search method based on the joint computation of two different functions: (i) semblance, used to measure the similarity among signals recorded by two or more stations [*Neidell and Taner*, 1971], and (ii) R^2, calculated on the basis of the spatial distribution of seismic amplitude (see *Cannata et al.* [2013] for further details). LP event sources in 2013 were similarly located to those obtained in the previous years [e.g., *Patanè et al.*, 2008; *Cannata et al.*, 2009, 2013], that is below the VOR-BN craters at shallow depths (> ~2 km above sea level (asl); Figures 5a and 5b). Moreover, if we consider only LP events with low-frequency peaks (<1.2 Hz) taking place during 29 April to 5 September (Figures 5c and 5d), there are no significant differences with the locations obtained during all of 2013.

The time variations of volcanic tremor, in terms of amplitude and source locations, were also investigated (Figures 2d, 6, and 7). In particular, the time evolution of its amplitude was followed by the RMS amplitude of the seismic signal recorded by the vertical component of ESLN station, calculated on 10 s long moving windows filtered in the band 0.5–2.5 Hz (Figure 2d). Since the seismic RMS depends not only on volcanic tremor but also on amplitude transients (LP events, volcano-tectonic earthquakes, regional earthquakes, and so on), we calculated the 25° percentile on 8 h long moving windows of RMS to exclude the contributions of amplitude transients and highlight the variations exclusively related to volcanic tremor changes. The most important RMS peaks, coinciding with the lava fountains, were observed during February–April and October–December periods. If we focus on the 25° percentile trends during the period in between the two lava fountain cycles, it is possible to observe a gradual increase in the volcanic tremor amplitude (particularly evident from June), which slightly reduced on 5 September. This amplitude reduction is visible in Figure 7a, focusing on the volcanic tremor features during 4–6 September.

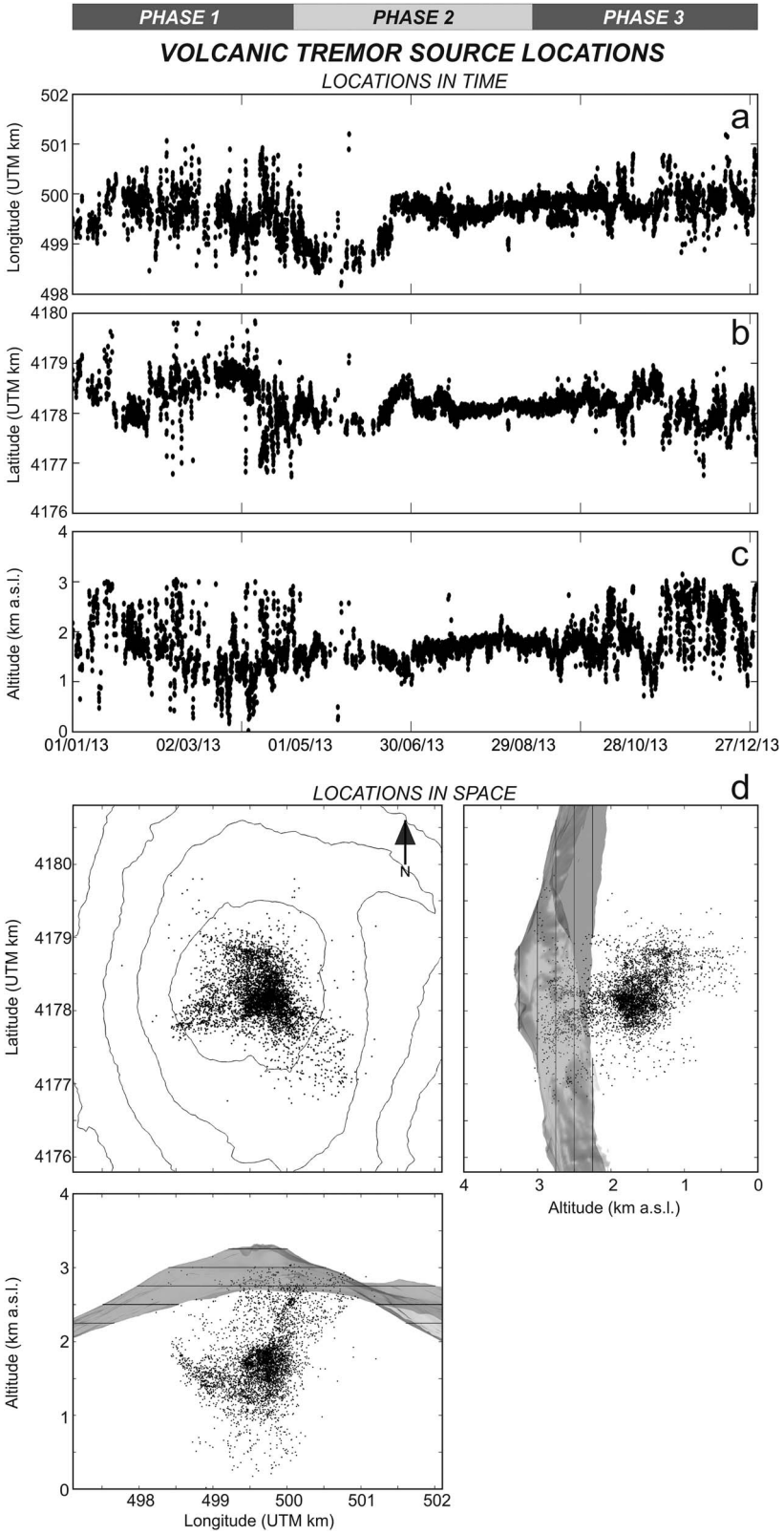

Figure 6. Volcanic tremor source locations. (a–c) Time variation of the location of the volcanic tremor centroids, obtained within 1 h long sliding windows during 2013 in the band 0.5–2.5 Hz. (d) Map and sections of Etna with the locations of the volcanic tremor centroids during 2013. The top dark and light grey rectangles indicate the time intervals called Phase 1, Phase 2, and Phase 3 (see section 4 for details).

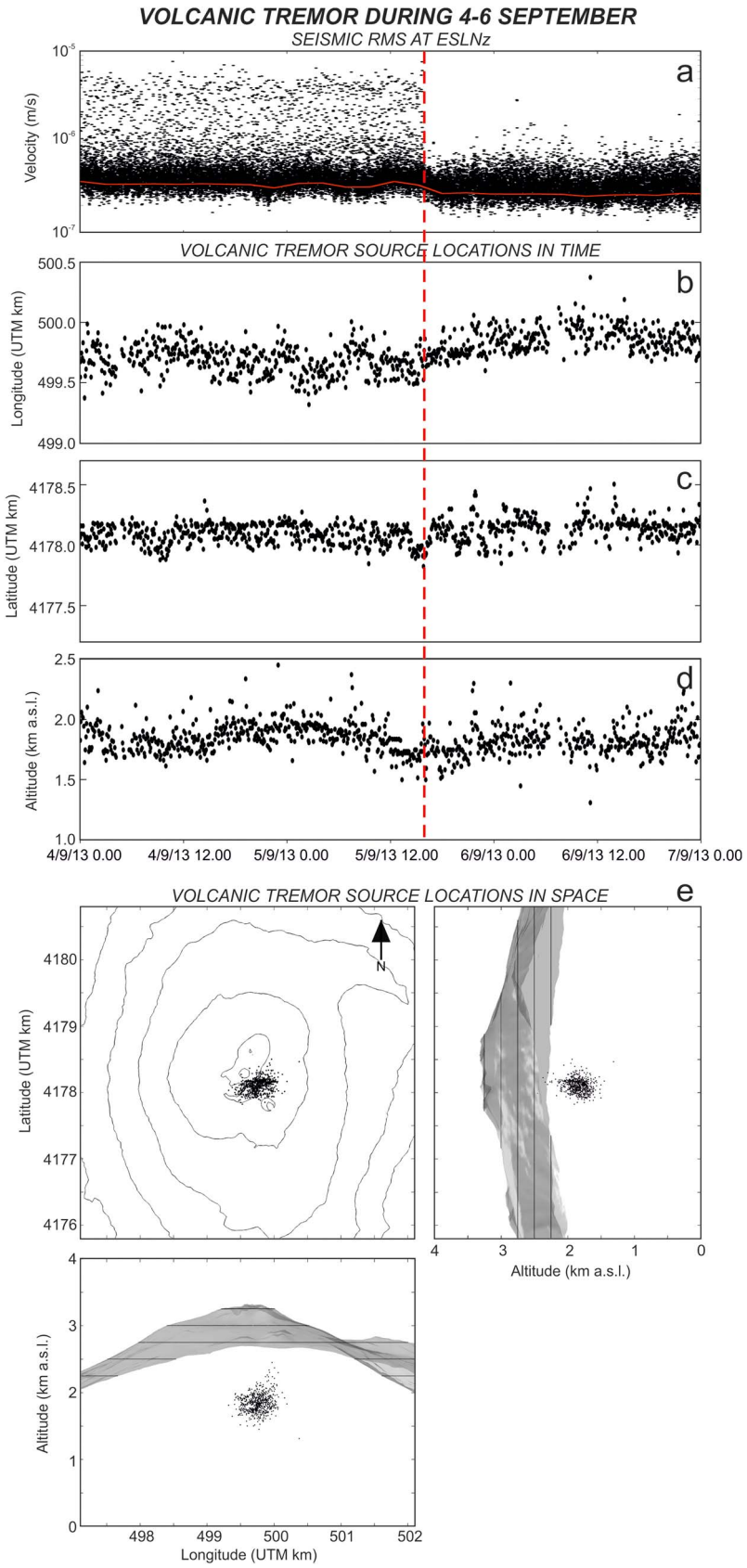
VOLCANIC TREMOR DURING 4-6 SEPTEMBER
SEISMIC RMS AT ESLNz
Velocity (m/s)
a
VOLCANIC TREMOR SOURCE LOCATIONS IN TIME
Longitude (UTM km)
b
Latitude (UTM km)
c
Altitude (km a.s.l.)
d
4/9/13 0.00
4/9/13 12.00
5/9/13 0.00
5/9/13 12.00
6/9/13 0.00
6/9/13 12.00
7/9/13 0.00
VOLCANIC TREMOR SOURCE LOCATIONS IN SPACE
e
N
Latitude (UTM km)
Altitude (km a.s.l.)
Altitude (km a.s.l.)
Longitude (UTM km)

Figure 7

Table 1. The 25°, 50°, and 75° Percentile Values Calculated on the Longitude, Latitude, and Altitude Errors Obtained in the Locations of the Volcanic Tremor Source Centroids

	Longitude (km)	Latitude (km)	Altitude (km)
25° percentile	0.70	0.39	1.08
50° percentile	0.74	0.42	1.14
75° percentile	0.79	0.45	1.18

The centroid of the volcanic tremor source was also located within 1 h long sliding time windows, by a grid-search method based on spatial seismic amplitude distribution, assuming propagation in a homogeneous medium (for details about the method see *Di Grazia et al*. [2006] and *Cannata et al*. [2013]) applied on the three-component seismic signals filtered in the frequency band 0.5–5.5 Hz. The variations in time and space of the volcanic tremor centroid locations are given in Figure 6, and show marked and swift changes during the eruptive lava fountain periods (February–April and October–December), while slight and gradual migrations can be observed during the intereruptive interval (May–September). Most of the calculated volcanic tremor centroids are located below the summit area at shallow depths (>1 km asl). In order to pinpoint eventual variations in the volcanic tremor location time related to the 5 September BN explosion, the locations of the volcanic tremor centroids were also obtained with a higher temporal resolution (5 min) in the interval 4–6 September. The location errors are given in Table 1. The results, shown in Figure 7, highlight a slight eastward migration of the volcanic tremor centroid from the BN area toward the SEC area (~0.3 km), taking place at the same time as the BN explosion and accompanying the slight decrease in the volcanic tremor amplitude (see the 25° percentile time series in Figure 7a). Although the amount of this shift is smaller than the location error, both the nondispersed nature of the location values and the aforementioned variations, taking place exactly at the same time as the BN explosion, suggest that a given source migration occurred. Hence, the eastward shift has to be taken into account, rather than the absolute locations before and after the explosion.

Finally, we investigated the seismic signal accompanying the 5 September BN explosion (Figure 3b). This signal is made up of a first part with minor amplitude and duration of ~20 s, a second part with higher amplitude and duration of about 15 s, and a coda. We located the first two parts by using the aforementioned method semblance + R^2. The results are presented in Figures 5c and 5d by two ellipsoids (the black and the red ones regarding the first and second parts of the explosion, respectively), whose sizes indicate the location errors. Such errors were calculated by using the method described by *Almendros and Chouet* [2003], based on both the space distribution of the goodness parameters (semblance + R^2 in this case) and the signal-to-noise ratio. It is clear that the source area of the 5 September BN explosion is the same as the LP event source area. Furthermore, it is worth noting that the source of the first part of the explosion was slightly deeper (about 2.500 ± 0.250 km asl) than the source of the second part (about 3.100 ± 0.125 km asl).

3.2. Infrasonic Data

The permanent infrasonic network is made up of 10 stations located at distances ranging from ~1 to 8 km from the center of the summit area (Figure 1c). Four stations are equipped with Monacor condenser microphones MC-2005, with a sensitivity of 80 mV/Pa in the 1–20 Hz infrasonic band, the others with GRASS 40AN microphones with a flat response at a sensitivity of 50 mV/Pa in the frequency range of 0.3–20,000 Hz. The infrasonic signals are acquired at a sampling rate of 50 Hz. As reported for the seismic networks, two of the infrasonic stations (EBEL and ETFI; see yellow circles in Figure 1c) were destroyed during the paroxysmal eruptive episodes of 28 February and 11 November 2013.

The detected infrasonic events were located by a grid-search technique based on the brightness function [e.g., *Kao and Shan*, 2004; *Cannata et al*., 2011, 2013], which allowed highlighting three different infrasonic source areas active during 2013: NEC, NSEC, and BN/VOR (Figure 8a). The NEC source has continuously emitted infrasonic events not only during 2013 (Figure 8e) but at least since the installation of the permanent infrasonic network in 2006 [e.g., *Sciotto et al*., 2011; *Spina et al*., 2014]. The activity of this source is related to

Figure 7. Volcanic tremor during 4–6 September. (a) RMS amplitude of the vertical component of the seismic signals recorded during 4–6 September 2013 by ESLN station and filtered in the band 0.5–2.5 Hz (black dots) and relative 25° percentile (red line). (b–d) Time variation of the location of the volcanic tremor centroids, obtained within 5 min long sliding windows during 4–6 September 2013 in the band 0.5–2.5 Hz. (e) Map and sections of Etna with the locations of the volcanic tremor centroids during 4–6 September 2013. The vertical dashed red line in Figures 7a–7d indicates the occurrence time of the explosion at BN, which took place on 5 September 2013 at 15:39.

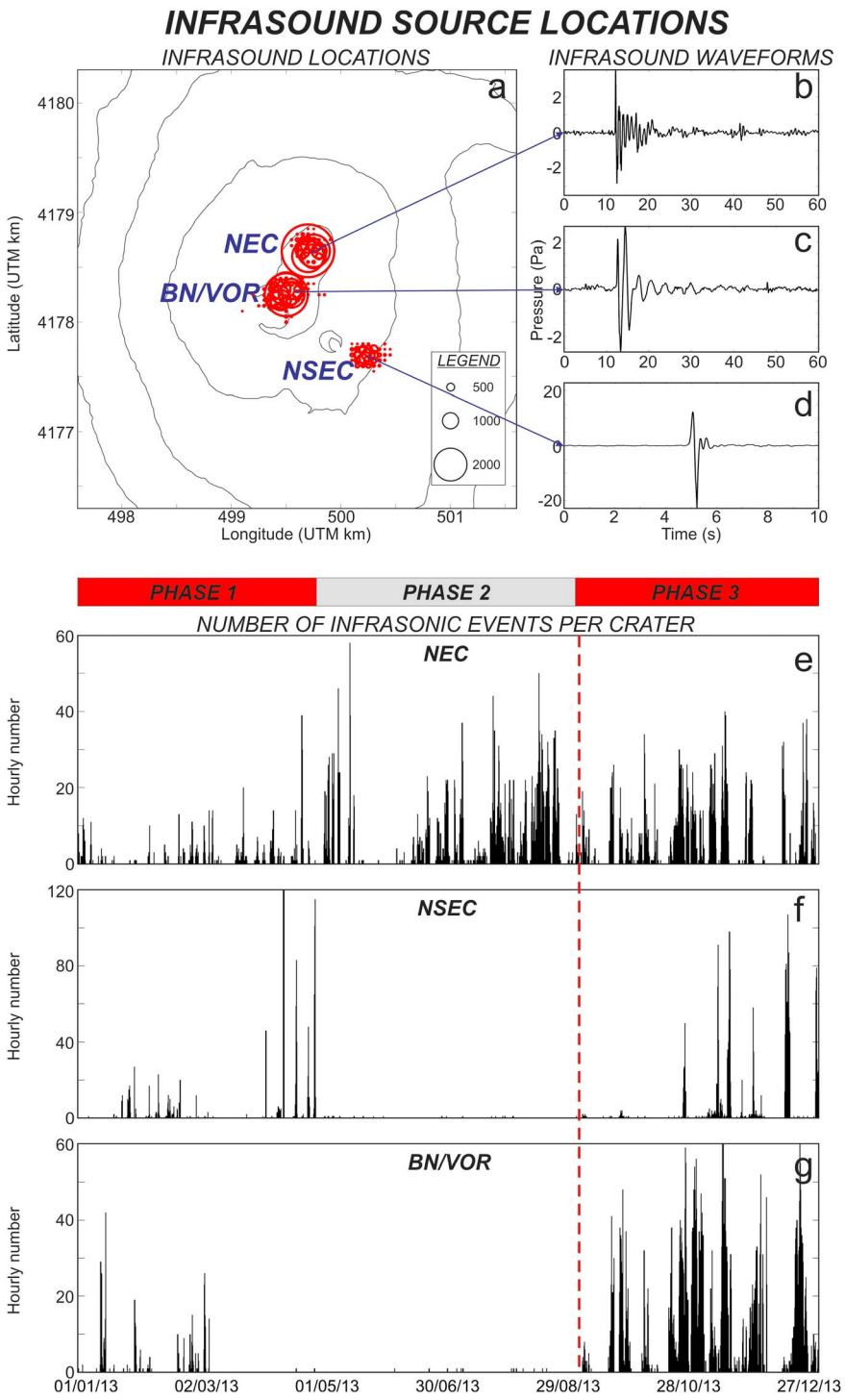

Figure 8. Infrasound source locations. (a) Map of Etna with the location of the infrasonic events recorded during 2013 (the radii of the red circles are proportional to the number of locations of infrasonic events in each grid node; see legend in the bottom right corner). (b–d) Waveforms of typical infrasonic events generated by NEC, BN, and NSEC, respectively. (e) Hourly number of infrasonic events located in the NEC area during 2013. (f) Hourly number of infrasonic events located in the NSEC area during 2013. (g) Hourly number of infrasonic events located in the BN/VOR area during 2013. The vertical dashed red line in Figures 8e–8g indicates the occurrence time of the explosion at BN, which took place on 5 September 2013 at 15:39. The top red and grey rectangles indicate the time intervals called Phase 1, Phase 2, and Phase 3 (see section 4 for details).

the voluminous, pulsating degassing that is characteristic for this crater. The infrasonic events produced by the NEC commonly last ~20–30 s and are characterized by relatively low frequency (generally <2 Hz; for details about the features of NEC events see *Spina et al*. [2014]) (Figure 8b). The NSEC generated infrasonic events during the periods of explosive activity (Figure 8f). NSEC events generally show spectral peaks at higher frequency (2–5 Hz) and shorter duration (<2 s) than NEC events (Figure 8d). Finally, the BN/VOR was active in terms of infrasonic radiation both during January–March and from 5 September (Figure 8g). In particular, during the former period the infrasonic activity was linked to the explosive activity of the BN and VOR, accompanying the first lava fountain cycle. From 5 September, a BN infrasonic source, associated with degassing processes, has been continuously active. A typical waveform of a BN infrasonic event recorded after 5 September shows a spectral content at frequencies <1 Hz and duration of ~20–30 s (Figure 8c).

3.3. Tilt and GPS Data

The Etna permanent tilt network comprises 14 biaxial electronic instruments installed in shallow boreholes at 3–30 m [*Ferro et al*., 2011; *Gambino et al*., 2014 for more details]. Roughly speaking, a tilt component, named radial, is directed toward the central craters and a positive signal change indicates crater up, while a second component (tangential) is oriented orthogonally. Resolution of instruments installed on Etna covers 0.005–0.1 μrad, mainly appreciable during rapid (minutes to few hours) tilt changes [*Gambino et al*., 2007; *Bonaccorso et al*., 2011]. Over long-term periods (months/year) small variations may be masked by environmental noise due to temperature, rainfalls, seismicity, and local effects [e.g., *Bonaccorso et al*., 1999]. Seasonal temperature effects may be reduced through linear regression with temperature data [e.g., *Bonaccorso*, 1996].

We considered the data of CDV (Figure 1d), which, unlike other stations, shows tilt and ground temperature at 1.5 m depth highly correlated to each other. This allowed us to correct the tilt data through linear regression with temperature data and hence to appreciate long-term changes in the order of 1.0–1.5 μrad [*Allard et al*., 2006; *Patanè et al*., 2013]. CDV during 2013 recorded clear signals due to an inflation (about 4.0 μrad) of the edifice from end of February to beginning of March to 5 September (Figure 2f). Successively, the inflation ended and a clear deflation trend started a few weeks after.

At Etna, the GPS permanent network began to operate in November 2000. Since then, the permanent network has been improved, reaching the current configuration of 39 stations that cover a large part of the volcanic edifice (Figure 1d). As reported for the seismic and infrasonic networks, one of the GPS stations (ETFI; see yellow circle in Figure 1d) was destroyed during the paroxysmal eruptive episode of 11 November 2013. The daily raw observations, collected from the GPS permanent network for the whole 2013, were processed using the GAMIT/GLOBK software [*Herring et al*., 2010] following the strategy described in *Gonzalez and Palano* [2014]. Estimated GPS daily time series and geodetic velocities for specified time intervals were referred to the "Etn@ref" reference frame (a local reference frame computed to isolate the Etna's volcanic deformation from the background tectonic pattern; see *Palano et al*. [2010] for details).

To detect significant signals related to Etna's activity we analyzed the daily baseline changes for the sites ECNE and EINT because they were quasi-continuously operating throughout the investigated time interval (Figure 2g). Moreover, this baseline crosses the crater area along an approximately NS direction and is sensitive to any change of the deformation pattern of the volcano [e.g., *Aloisi et al*., 2011; *Spampinato et al*., 2015]. Visual inspection of the time series of ECNE-EINT baseline length, spanning the 1 January to 31 December 2013 time interval, allows us to detect at least six different ground deformation stages (Figure 2g). In particular, the baseline does not show significant change from 1 January to 14 February while lengthened by ~0.6 cm from 2 May to 25 October, respectively. The baseline shortened by ~2.5 cm, ~2.0 cm, and ~1.0 cm from 15 February to 26 February, from 2 April to 1 May, and from 26 October to 31 December, respectively. These periods characterized by baseline shortening mostly coincided with the intervals of occurrence of lava fountains (for instance, the first lava fountain episode of the second cycle took place on 26 October).

During 27 February to 1 April, the baseline length does not show any significant change with the exception of slight lengthening (~0.2 cm) that occurred in the last week of March. In the following we focus on the 2 May to 25 October time interval; the estimated surface ground velocity field reported in Figure 9 is characterized by a general radial pattern, clearly depicting a slight inflation of the volcano edifice. The difference in the date of the end of inflation between tilt and GPS data (5 September and 25 October) can be due to the fact that tilt is more sensitive to very slight ground deformations than GPS.

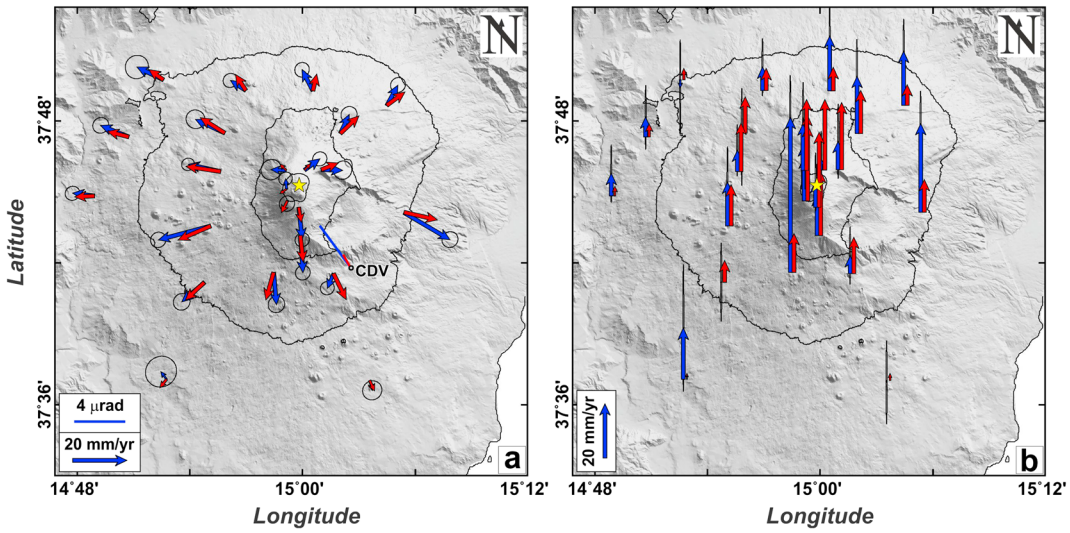

Figure 9. Observed (blue arrows) and expected (red arrows) (a) horizontal and (b) vertical GPS velocities as computed for the 2 May to 25 October 2013 time interval. Uncertainties associated to GPS velocities are at the 95% level of confidence. Observed (blue) and modeled (red) tilt signals for station CDV, spanning the same time interval, are also reported. The yellow star indicates the surface projection of modeled source.

This ground velocity field was used as input to constrain isotropic half-space elastic inversion models. Values of 30 GPa and 0.25 were assumed for the shear modulus and Poisson's ratio in the half-space, respectively; the chosen rigidity represents an average value for Etna's crust [*Chiarabba et al*., 2000] and corresponds to a typical value commonly used in modeling works for Mount Etna [e.g., *Palano et al*., 2008; *Bonanno et al*., 2011]. In the computation, both horizontal and vertical GPS components were inverted by taking into account weights proportional to the associated velocity uncertainties. Moreover, we included in the inversion also the tilt measurement at CDV station with the same weight as the GPS velocities. We compared two different analytical pressure source models, the simpler Mogi source [*Mogi*, 1958] with four free parameters and the more general Yang source [*Yang et al*., 1988] which has seven free and separable parameters considering the relationship in *Tiampo et al*. [2000] between pressure and volume of the reservoir. We tried also to invert even more complicated sources to consider simultaneously shallow and deep sources (e.g., two Mogi sources), but, even if the fit improved, the solutions were basically unrealistic in their locations. We performed the model estimation from the observed ground velocity pattern by using the genetic algorithm approach [*Tiampo et al*., 2000], and, in addition, to include topography, we varied the depth of the source accordingly [*Williams and Wadge*, 2000]. Following the criterion described in *Cannavò* [2012], based on the evaluation of model residuals and global sensitivity of model parameters, we considered the Yang source for the further analysis because of its lower value of residuals chi-square (i.e., 5.0 instead of 6.5 for the Mogi source) and its lower sensitivity to data uncertainties (i.e., 0.53 of total first-order sensitivity index for Yang source instead of 0.82 for Mogi source). Estimation of the uncertainties in best fitting parameters was performed by adopting a Jackknife sampling method [*Efron*, 1982]. The estimated parameters of the modeled source are shown in Table 2. The modeled pressure source is located under the summit craters and well constrained at 95% of confidence between 8 and 9 km below sea level (bsl). The volume variation of the reservoir was estimated in $3.2 \cdot 10^6$ m^3 by limiting the ratio of pressure change to shear modulus within the elastic limits of the surrounding rock [*Lisowski et al*., 2008].

Table 2. Estimated Parameters for Yang Magmatic Pressure Source[a]

East UTM	499,426 ± 35 m
North UTM	4,178,623 ± 20 m
Depth	8412 ± 260 m
Δvolume	$3.2 \pm 0.16\ 10^6$ m^3
Axis ratio	0.24 ± 0.01
Strike	176 ± 5°
Plunge	10 ± 9°

[a]See *Yang et al*. [1988] and *Tiampo et al*. [2000] for parameter descriptions.

3.4. CO_2 Soil Degassing

With focus on the possible pressurization within the Etna plumbing system,

examining the variation in the degassing state of the volcano during the specified interval offers an important insight. In this work, we use geochemical data from the EtnaGas CO_2 soil flux network, which comprises 15 automatic stations (Figure 1e). These provide an almost homogenous coverage of the volcano flanks and have been specifically located in sites that are characterized by significant soil CO_2 emissions. The monitoring stations of the network were entirely developed by INGV Palermo and are able to monitor parameters such as CO_2 and CH_4 soil fluxes, atmospheric temperature, pressure, humidity, rain, wind speed, and wind direction. All the stations were time-synchronized, and the data were recorded hourly, locally stored, and transmitted daily to the laboratory in Palermo by GSM or radio links. CO_2 flux measurements are carried out by the dynamic method [*Gurrieri and Valenza*, 1988; *Gurrieri et al*., 2008, and reference therein], in which the CO_2 content in a mixture of air and soil gas is obtained by means of a probe inserted into the soil at a depth of 50 cm. In accordance with the method proposed in *Liuzzo et al*. [2013], we consider here the same data processing approach to obtain a unified CO_2 flux signal from all the monitoring stations of the network. In this method, three steps are considered: first, each time series from all the stations is filtered for the meteorological parameters and/or seasonal variations; second, in order to compare the amplitude of the CO_2 flux variation from different stations, each soil CO_2 flux series is normalized within the range of 0–1; and finally, all the time series from each station are added together and the final sum is normalized again within the interval 0–1 (more details on the method in *Liuzzo et al*. [2013]).

The results are shown as Φ_{Norm} in Figure 2h, representing the total soil CO_2 flux amplitude variations at a specific time (no longer giving any CO_2 flux measurement units), where a high value of Φ_{Norm} implicitly suggests a high degassing state on Etna. In order to treat the entire EtnaGas network data series homogeneously, the data were processed from the period spanning January 2011 to January 2015, which is a longer period than that considered in this work (only 2013). In fact, Figure 2h shows that during 2013 the degassing state on Etna reached a maximum amplitude of CO_2 flux variation, and although the entire series is not shown, it was actually the highest value reached in 4 years. Furthermore, during 2013 the Φ_{Norm} showed a considerable variation which peaked on 3 September after a fairly steady increase. Following this, EtnaGas network recorded a sharp Φ_{Norm} decrease, which lasted until the end of October, while from November to the end of the year the Φ_{Norm} remained fairly stable at a medium amplitude value without reaching the minimum.

CO_2 flux variations in volcanic environments have been linked to the rising of volatile-rich magmas as a consequence of the release of gas in disequilibrium with decreasing pressure. CO_2 is one of the most abundant among these gases in magma content and one of the earliest to be released, starting from a pressure value of 500–400 MPa and becoming particularly efficient under the value of 200–150 MPa [*Holloway and Blank*, 1994; *Lesne et al*., 2011]. Taking this into consideration, it is therefore reasonable to assume that during 2013 a significant pressurization in relation to the CO_2 flux occurred within the Etna plumbing system which peaked during the first few days of September. According with the pressure-related CO_2 solubility in the magma, the high value reached in September presumably involved part of the plumbing system at a pressure below 200–150 MPa (corresponding to depth lower than 7 km bsl), which is a pressure where the CO_2 release is more efficient. These results are also reasonably compatible with the range of depth inferred by tilt and GPS data modeling, considering the fact that the deeper GPS source is related to the ingression of the magma batch with most of its volatile content still present in solution. It is worth noting the almost simultaneous change in the degassing state of the plumbing system, the ground deformation pattern (mainly highlighted by the tilt data), and the occurrence of the BN explosion on 5 September. Synchronized changes in both ground deformation and geochemical time series have been previously observed at Mount Etna [e.g., *Aiuppa et al*., 2010] as well as at other volcanoes (e.g., Asama [*Kazahaya et al*., 2015]).

4. Discussion

In this paper, we applied a multiparametric approach, combining volcanological, seismic, infrasonic, tilt, GPS, and geochemical data, to investigate the dynamics of Mount Etna during 2013.

The cartoon in Figure 10 summarizes the main phases of volcano activity described in this section. The eruptive activity during 2013 took place in two cycles, February–April and September–December (named "phase 1" and "phase 3" in Figure 10). The former cycle was characterized by the most intense eruptive activity that occurred at Etna in recent years. Indeed, the beginning of the first cycle of lava fountains was characterized by

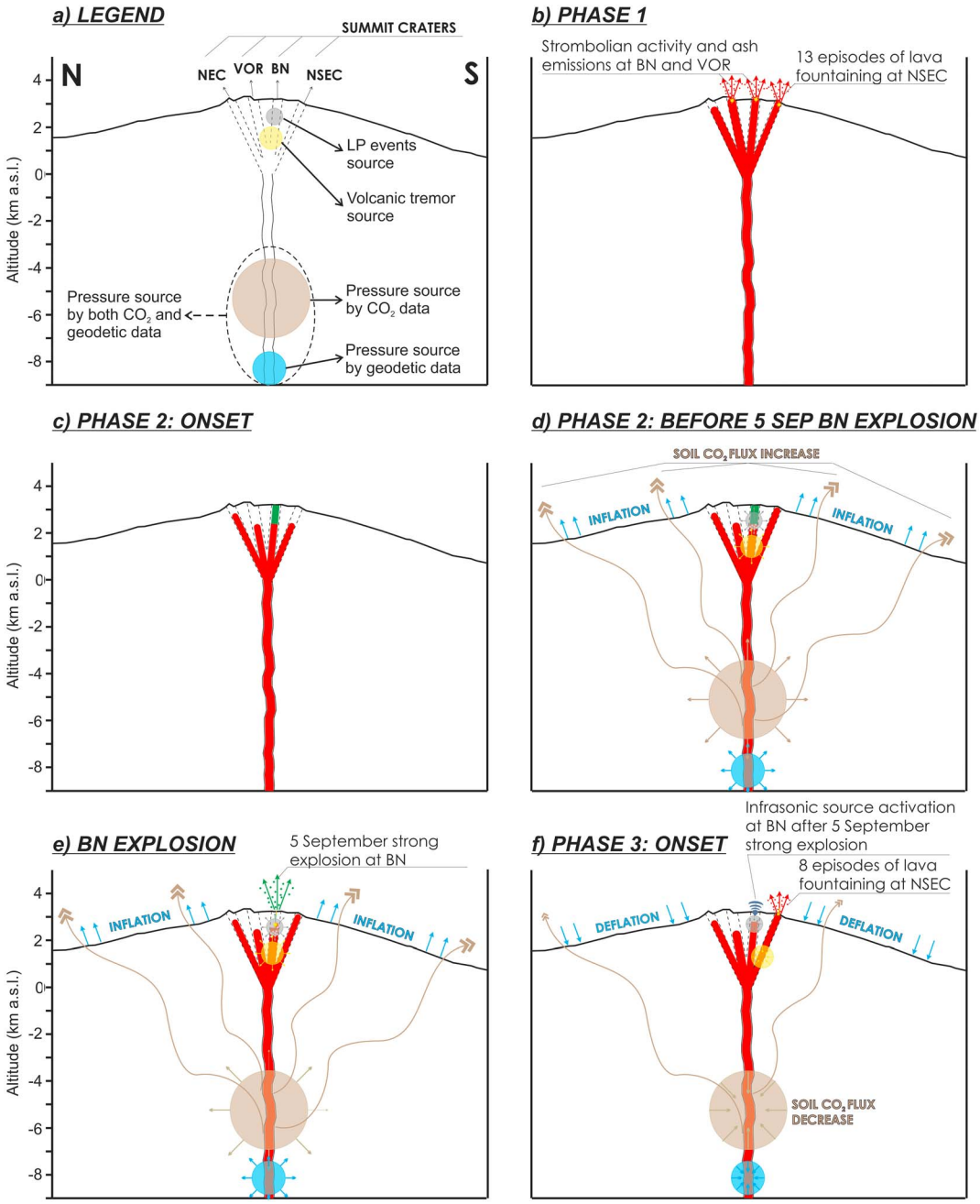

Figure 10. Cartoon showing the different phenomena taking place at Etna during 2013. (a) Legend, indicating the location of the summit craters and the sources, composing the plumbing system, identified in 2013. The dashed lines, displaying the upper part of the plumbing system, indicate the lack of knowledge on the precise geometry and links of the plumbing system. (b) Phase 1, characterized by Strombolian activity at VOR and BN, and by lava fountaining at NSEC. (c) Onset of Phase 2, characterized by the presence of a plug (indicated by the green area and formed during 2012 to first months of 2013), composed of solidified lava flows in the upper portion of the BN plumbing system. (d) Phase 2, before the 5 September BN explosion, characterized by inflation caused by a pressure source at ~8–9 km bsl, CO_2 flux increases, due to a pressure source at ~3–6 km bsl, increases in the energy of volcanic tremor and LP event sources located at 1–3 km asl. The outward arrows in the different sources indicate the pressurization of the different portions of the plumbing system. (e) BN explosion, which occurred on 5 September 2013 and caused the expulsion of the BN plug. (f) Phase 3, characterized by deflation, decrease in CO_2 flux, activation of a new steady infrasonic source at BN, slight shift of the volcanic tremor source toward NSEC, and gradual restart of eruptive activity at NSEC. The inward arrows in the distinct sources indicate the depressurization of the different portions of the plumbing system.

the highest rate of occurrence of paroxysmal episodes (up to two in a single day) since the onset of the lava fountaining activity on 12 January 2011 and by simultaneous activity at three summit craters at the same time (NSEC, BN, and VOR; Figure 10b).

The period between the two cycles of paroxysmal activity (named "phase 2" in Figure 10) was characterized by important variations involving seismic, geodetic, and geochemical signals (Figures 10c and 10d). In particular, from the beginning of May, we observed LP events with low-frequency content (peak frequencies $<$1.0 Hz; Figure 2c). Such sharp spectral changes, coinciding with the end of the first lava fountain cycle, can be due to variations in the geometrical features of the plumbing system and/or properties of the fluids filling it [e.g., *Kumagai and Chouet*, 2000, 2001]. Moreover, a decrease in the spectral peak was observed from May to the end of August (from ~1.0 to ~0.6 Hz; Figure 2c). Due to the gradual character of this change, we can suppose that it was caused by a slow change in the chemico-physical properties of the fluids filling the shallow part of the plumbing system, corresponding with the LP source locations ($>$2 km asl; Figure 5). Moreover, the same time period was characterized by increases in amplitudes of both LP events and volcanic tremor (Figures 2b and 2d, respectively). Similar changes in volcanoes have been interpreted as caused by pressurization of the plumbing system that sometimes preceded eruptions such as at Redoubt [*Chouet et al*., 1994], Mount St. Helens [*Moran et al*., 2008], Colima [*Varley et al*., 2010], and Etna [*Bonaccorso et al*., 2011]. Since the source of both LP events and volcanic tremor are shallow ($>$1 km asl), we can infer that from May to the beginning of September at least the shallow portion of the Etna plumbing system was becoming progressively pressurized. Since the increases of amplitude of both LP events and volcanic tremor were more evident from the end of June (Figures 2b and 2d), the pressurization process was particularly relevant after that time. By means of the geodetic and geochemical data (Figures 2f–2h), we can recognize that the LP event and volcanic tremor amplitude increases are only superficial evidence of a broader pressurization process involving the whole plumbing system at least from 3 to 9 km bsl (Figure 10d). This range comprises the pressure source depths obtained by both geodetic and CO_2 data. By means of the geodetic modeling, the estimated pressure increase corresponds to a volume increase of ~$3 \cdot 10^6$ m^3 (Table 2).

Similar evidence was observed at Etna during the second half of 2010, when the LP amplitudes gradually increased [*Patanè et al*., 2013], accompanied by volcano inflation [*Patanè et al*., 2013] and CO_2 flux increase [*Liuzzo et al*., 2013]. Similar to what we observed from late April to early September 2013, such a behavior in 2010 suggested the pressurization of the Etna plumbing system, which indeed led to the onset of the 2011 lava fountaining activity [*Liuzzo et al*., 2013; *Patanè et al*., 2013].

The explosion, which occurred at the BN at 15:39 on 5 September 2013, instantaneously modified the trends of many of the aforementioned signals (Figures 10e and 10f). First of all, the LP events characterized by low-frequency content disappeared (Figure 2c). The change was so sharp that only a rather sudden modification in the plumbing system, caused by the explosion, can justify it. According to LP/VLP event source models, the generation of these signals could require geometrical discontinuities along the magmatic transport system such as changes in conduit diameter, pipe elbow, and interlocking cracks [e.g., *James et al*., 2006; *Chouet et al*., 2010]. On this basis, we can suppose that the LP events (at least the ones characterized by low-frequency content, observed during end of April to beginning of September) were due to a given discontinuity within the shallow plumbing system, which was destroyed by the explosion putting an end to this kind of events. Furthermore, the second part of the explosion, characterized by the highest amplitude (Figure 3b) and located at very shallow depth (Figure 5d), could be interpreted as the seismic signature of the expulsion of the BN plug, composed of solidified lava flows, that was replaced by a depression (see pictures in Figure 4).

After the explosion, sharp decreases in the amplitude of both LP events and volcanic tremor were observed (Figures 2b, 2d, and 7a), suggesting a fast depressurization of the shallow portion of the plumbing system ($>$1 km asl). Moreover, the explosion gave rise to a new steady source of infrasonic events located within the BN (Figures 8a and 8g), in correspondence with the newly formed pit depression (see picture in Figure 4b). This pit depression should therefore represent the shallowest part of the plumbing system, which has generated the new infrasonic events since 5 September and had probably produced the LP events with low-frequency content during end of April to beginning of September. On the basis of these considerations, it is also probable that the BN explosion was caused by the aforementioned plumbing system pressurization taking place from the end of April. Right after the BN explosion also the tilt and CO_2 trends sharply changed (Figures 2f and 2h), testifying the end of the pressurization phase and successively the beginning of the

depressurization. This suggests that the BN explosion did not only affect the shallow part of the plumbing system but also influenced the deeper portions of the magma transport system at least down to the pressure sources highlighted by geodetic and geochemical data (3–9 km bsl). In particular, as for the tilt data, the inflation observed up to 5 September was replaced by a steady trend, and successively by deflation, which heralded the return of episodic lava fountaining in late October and continued to the end of 2013 (see supporting information for the estimated GPS deformation pattern, covering the 25 October to 31 December 2013 time interval). Indeed, a few hours after the BN explosion the explosive activity at NSEC intensified. On the basis of this evidence, we infer that the plug expulsion caused the depressurization of the shallow plumbing system, that quickly propagated downward, triggering uprises of magma/gas. A similar phenomenon of downward propagating decompression was observed in 2010 at Eyjafjallajökull volcano [*Tarasewicz et al*., 2012]. Indeed, according to these authors, the systematic downward migration of seismicity was explained by the downward propagation of a decompression wave that triggered magma release from progressively deeper sills.

Since the BN plug expulsion was crucial in the volcano activity, starting the depressurization phase, it can be inferred that the plug formation (due to the BN eruptive activity during 2012 to first months of 2013) likely played an important role also in the pressurization phase. It is probable that this plug, partially preventing or limiting the BN degassing activity, created the conditions for the plumbing system pressurization.

The clear time relationship between the 5 September 2013 BN explosion and the intensification of NSEC activity highlights without doubt the link between the plumbing systems feeding the two craters.

The complex relationships between the summit craters of Etna and the characteristics of the superficial plumbing system of the volcano have been intriguing scientists for decades [*Chester et al*., 1985; *Allard et al*., 2005; *Spina et al*., 2014]. For at least the past 20 years, the BN seems to have been a particular indicator of the state of the volcano, being often the first crater to reopen after an extended period of eruptive quiescence. This was so in the summer of 1995, when summit eruptive activity resumed at the BN after 2 years of quiescence following the major 1991–1993 flank eruption [e.g., *Rothery et al*., 2001; *Allard et al*., 2005]. An intensification of the BN activity in November 1996 was instantly followed by the reawakening of SEC after 5 years of repose [*Rothery et al*., 2001]. Again, after the 2001 flank eruption, the first signs of renewed eruptive activity, a few months later, were first heard and then seen at the BN [*Andronico et al*., 2005]. It was thus evident that the BN was, at least in certain periods, rather sensitive to the dynamics of, and most notably, pressure changes in Etna's shallow plumbing system.

In 2010–2013, the association of eruptive activity at the BN and at the NSEC was often rather intimate. Both craters showed a gradual increase in explosive (phreatomagmatic) activity during 2010, before the start of episodic lava fountaining at the NSEC in January 2011. When the frequency of paroxysmal eruptive episodes at the NSEC increased in the summer of 2011 (from one episode every 1–2 months in January–June to three to four episodes per month during July–September), Strombolian activity started also in the BN in July, the first significant magmatic activity at that crater for 10 years [*Patanè et al*., 2013]. In early 2012, some paroxysmal episodes at the NSEC were accompanied or followed by ash emissions from the BN. However, in July 2012, Strombolian activity started at the BN after episodic lava fountaining at the NSEC had entered into a 10 month long pause, and in January–February 2013, eruptive episodes alternated at the BN and the NSEC, rather than occurring contemporaneously (see reports on the INGV–Osservatorio Etneo website), whereas the BN ceased erupting when activity started at the Voragine in late February 2013.

The peculiar relationship between the BN and the NSEC became again evident in April–May 2015, when an explosion from the former on 12 April—much smaller than the 5 September 2013 event—was followed 1 month later by a new eruptive episode at the latter, which in turn was accompanied by several strong ash emissions from the BN.

5. Concluding Remarks

The following points summarize the main conclusions:

1. the time interval in between the two 2013 lava fountain cycles at Mount Etna (end of April to beginning of September) was characterized by a gradual pressurization of both deep and shallow plumbing system portions (from ~3 to 9 km bsl to the summit), culminating with the 5 September 2013 BN explosion;

2. the 5 September 2013 BN explosion sharply and suddenly modified the plumbing system, giving rise to open conduit conditions at BN (suggested by the activation of a new infrasound source), put an end to the pressurization, and caused a depressurization of the shallow plumbing system, that quickly propagated downward triggering uprises of magma/gas;
3. the pattern changes, observed in different time series and time related to the 5 September 2013 BN explosion, testify how a shallow phenomenon can affect the entire plumbing system down to some kilometers below sea level;
4. the clear time relationship between the 5 September 2013 BN explosion and the NSEC activity intensification highlights the close link between plumbing systems feeding the two summit craters.

Acknowledgments

We are grateful to Michael Lisowski, an anonymous reviewer, and the Associate Editor for their useful suggestions that greatly improved the paper. We are indebted to the technicians of the INGV–Osservatorio Etneo for enabling the acquisition of seismic, infrasonic, tilt, and GPS data. We also thank Biagio Ragonese for providing us the BN picture. This work was partially funded by DPC-INGV 2014 and by PON01_00683 SIGMA project. The original data used in this manuscript are available from these authors: A. Cannata for seismic and infrasonic data (andrea.cannata@ingv.it), M. Palano and F. Cannavò for GPS data (mimmo.palano@ingv.it and flavio.cannavo@ingv.it), S. Gambino for tilt data (salvatore.gambino@ingv.it), and M. Liuzzo for CO_2 flux data (marco.liuzzo@ingv.it).

References

Aiuppa, A., et al. (2010), Patterns in the recent 2007–2008 activity of Mount Etna volcano investigated by integrated geophysical and geochemical observations, *Geochem. Geophys. Geosyst.*, *11*, Q09008, doi:10.1029/2010GC003168.

Allard, P., M. Burton, and F. Murè (2005), Spectroscopic evidence for a lava fountain driven by previously accumulated magmatic gases, *Nature*, *433*, 407–410, doi:10.1038/nature03246.

Allard, P., B. Behncke, S. D'Amico, M. Neri, and S. Gambino (2006), Mount Etna 1993–2005: Anatomy of an evolving eruptive cycle, *Earth Sci. Rev.*, *78*, 85–114.

Almendros, J., and B. Chouet (2003), Performance of the radial semblance method for the location of very long period volcanic signals, *Bull. Seismol. Soc. Am.*, *93*, 1890–1903.

Aloisi, M., M. Mattia, C. Ferlito, M. Palano, V. Bruno, and F. Cannavò (2011), Imaging the multi-level magma reservoir at Mt. Etna volcano (Italy), *Geophys. Res. Lett.*, *38*, L16306, doi:10.1029/2011GL048488.

Alparone, S., A. Cannata, S. Gambino, S. Gresta, V. Milluzzo, and P. Montalto (2010), Time-space variation of volcano-seismic events at La Fossa (Vulcano, Aeolian Islands, Italy): New insights into seismic sources in a hydrothermal system, *Bull. Volcanol.*, *72*, 803–816, doi:10.1007/s00445-010-0367-6.

Andronico, D., et al. (2005), A multi-disciplinary study of the 2002–03 Etna eruption: Insights into a complex plumbing system, *Bull. Volcanol.*, *67*, 314–330, doi:10.1007/s00445-004-0372-8.

Andronico, D., M. D. Lo Castro, M. Sciotto, and L. Spina (2013), The 2010 ash emissions at the summit craters of Mt Etna: Relationship with seismo-acoustic signals, *J. Geophys. Res. Solid Earth*, *118*, 51–70, doi:10.1029/2012JB009895.

Behncke, B., S. Branca, R. A. Corsaro, E. De Beni, L. Miraglia, and C. Proietti (2014), The 2011–2012 summit activity of Mount Etna: Birth, growth and products of the new SE crater, *J. Volcanol. Geotherm. Res.*, *270*, 10–21, doi:10.1016/j.jvolgeores.2013.11.012.

Bonaccorso, A. (1996), Dynamic inversion of ground deformation data for modelling volcanic sources (Etna 1991–93), *Geophys. Res. Lett.*, *23*(5), 451–454, doi:10.1029/96GL00418.

Bonaccorso, A., G. Falzone, and S. Gambino (1999), An investigation into shallow borehole tiltmeters, *Geophys. Res. Lett.*, *26*(11), 1637–1640, doi:10.1029/1999GL900310.

Bonaccorso, A., A. Cannata, R. A. Corsaro, G. Di Grazia, S. Gambino, F. Greco, L. Miraglia, and A. Pistorio (2011), Multidisciplinary investigation on a lava fountain preceding a flank eruption: The 10 May 2008 Etna case, *Geochem. Geophys. Geosyst.*, *12*, Q07009, doi:10.1029/2010GC003480.

Bonanno, A., M. Palano, E. Privitera, S. Gresta, and G. Puglisi (2011), Magma intrusion mechanisms and redistribution of seismogenic stress at Mt. Etna volcano (1997–1998), *Terra Nova*, *23*, 339–348, doi:10.1111/j.1365-3121.2011.01019.x.

Cannata, A., M. Hellweg, G. Di Grazia, S. Ford, S. Alparone, S. Gresta, P. Montalto, and D. Patanè (2009), Long period and very long period events at Mt. Etna volcano: Characteristics, variability and causality, and implications for their sources, *J. Volcanol. Geotherm. Res.*, *187*, 227–249, doi:10.1016/j.jvolgeores.2009.09.007.

Cannata, A., M. Sciotto, L. Spampinato, and L. Spina (2011), Insights into explosive activity at eruptive fissure closely-spaced eruptive vents using infrasound signals: Example of Mt. Etna 2008 eruption, *J. Volcanol. Geotherm. Res.*, *208*, 1–11, doi:10.1016/j.jvolgeores.2011.09.003.

Cannata, A., G. Di Grazia, M. Aliotta, C. Cassisi, P. Montalto, and D. Patanè (2013), Monitoring seismo-volcanic and infrasonic signals at volcanoes: Mt. Etna case study, *Pure Appl. Geophys.*, *170*, 1751–1771, doi:10.1007/s00024-012-0634-x.

Cannavó, F. (2012), Sensitivity analysis for volcanic source modeling quality assessment and model selection, *C. R. Geosci.*, *44*, 52–59, doi:10.1016/j.cageo.2012.03.008.

Chaussard, E., F. Amelung, and Y. Aoki (2013), Characterization of open and closed volcanic systems in Indonesia and Mexico using InSAR time series, *J. Geophys. Res. Solid Earth*, *118*, 3957–3969, doi:10.1002/jgrb.50288.

Chester, D. K., A. M. Duncan, J. E. Guest, and C. R. J. Kilburn (1985), *Mount Etna: The Anatomy of a Volcano*, Chapman and Hall, London, U. K.

Chiarabba, C., A. Amato, E. Boschi, and F. Barberi (2000), Recent seismicity and tomographic modeling of the Mount Etna plumbing system, *J. Geophys. Res.*, *105*(B5), 10,923–10,938, doi:10.1029/1999JB900427.

Chouet, B. A., R. A. Page, C. D. Stephens, J. C. Lahr, and J. A. Power (1994), Precursory swarms of long-period events at Redoubt Volcano (1989–1990), Alaska: Their origin and use as a forecasting tool, *J. Volcanol. Geotherm. Res.*, *62*, 95–135, doi:10.1016/0377-0273(94)90030-2.

Chouet, B. A., P. B. Dawson, M. R. James, and S. J. Lane (2010), Seismic source mechanism of degassing bursts at Kilauea Volcano, Hawaii: Results from waveform inversion in the 10–50 s band, *J. Geophys. Res.*, *115*, B09311, doi:10.1029/2009JB006661.

Di Grazia, G., S. Falsaperla, and H. Langer (2006), Volcanic tremor location during the 2004 Mount Etna lava effusion, *Geophys. Res. Lett.*, *33*, L04304, doi:10.1029/2005GL025177.

Efron, B. (1982), *The Jackknife, the Bootstrap and Other Resampling Plans*, Soc. for Ind. and Appl. Math., Philadelphia, Pa.

Ferro, A., S. Gambino, S. Panepinto, G. Falzone, G. Laudani, and B. Ducarme (2011), High precision tilt observation at Mt. Etna Volcano, Italy, *Acta Geophys.*, *59*(3), 618–632.

Gambino, S., O. Campisi, G. Falzone, A. Ferro, F. Guglielmino, G. Laudani, and B. Saraceno (2007), Tilt measurements at Vulcano Island, *Ann. Geophys.*, *50*, 233–247.

Gambino, S., G. Falzone, A. Ferro, and G. Laudani (2014), Volcanic processes detected by tiltmeters: A review of experience on Sicilian volcanoes, *J. Volcanol. Geotherm. Res.*, *271*, 43–54.

Gonzalez, P. J., and M. Palano (2014), Mt. Etna 2001 eruption: New insights into the magmatic feeding system and the mechanical response of the western flank from a detailed geodetic dataset, *J. Volcanol. Geotherm. Res.*, *274*, 108–121, doi:10.1016/j.jvolgeores.2014.02.001.

Gurrieri, S., and M. Valenza (1988), Gas transport in natural porous mediums: A method for measuring CO_2 flows from the ground in volcanic and geothermal areas, *Rend. Soc. Ital. Mineral. Petrol.*, *43*, 1151–1158.

Gurrieri, S., M. Liuzzo, and G. Giudice (2008), Continuous monitoring of soil CO_2 flux on Mt. Etna: The 2004–2005 eruption and the role of regional tectonics and volcano tectonics, *J. Geophys. Res.*, *113*, B09206, doi:10.1029/2007JB005003.

Herring, T. A., R. W. King, and S. C. McClusky (2010), *Introduction to GAMIT/GLOBK, Release 10.4*, pp. 1–48, Mass. Inst. of Technol., Cambridge, Mass.

Holloway, J. R., and J. G. Blank (1994), Application of experimental results to C–O–H species in natural melts, in *Volatiles in Magmas, Reviews in Mineralogy*, edited by M. R. Carroll and J. R. Holloway, pp. 185–230, Mineralog. Soc. of Am., Washington, D. C.

James, M. R., S. J. Lane, and B. A. Chouet (2006), Gas slug ascent through changes in conduit diameter: Laboratory insights into a volcano-seismic source process in low-viscosity magmas, *J. Geophys. Res.*, *111*, B05201, doi:10.1029/2005JB003718.

Kao, H., and S. J. Shan (2004), The source-scanning algorithm: mapping the distribution of seismic sources in time and space, *Geophys. J. Int.*, *57*, 589–594.

Kazahaya, R., Y. Aoki, and H. Shinohara (2015), Budget of shallow magma plumbing system at Asama Volcano, Japan, revealed by ground deformation and volcanic gas studies, *J. Geophys. Res. Solid Earth*, *120*, 2961–2973, doi:10.1002/2014JB011715.

Kilburn, C. R. J., and B. Voight (1998), Slow rock fracture as eruption precursor at Soufriere Hills volcano, Montserrat, *Geophys. Res. Lett.*, *25*(19), 3665–3668, doi:10.1029/98GL01609.

Kumagai, H., and B. A. Chouet (2000), Acoustic properties of a crack containing magmatic or hydrothermal fluids, *J. Geophys. Res.*, *105*(B11), 25,493–25,512, doi:10.1029/2000JB900273.

Kumagai, H., and B. A. Chouet (2001), The dependence of acoustic properties of a crack on the resonance mode and geometry, *Geophys. Res. Lett.*, *28*(17), 3325–3328, doi:10.1029/2001GL013025.

Lesne, P., S. C. Kohn, J. Blundy, F. Witham, R. E. Botcharnikov, and H. Behrens (2011), Experimental simulation of closed-system degassing in the system basalt-H_2O-CO_2-S-Cl, *J. Petrol.*, *52*, 1737–1762, doi:10.1093/petrology/egr027.

Lisowski, M., D. Dzurisin, R. P. Denlinger, and E. Y. Iwatsubo (2008), Analysis of GPS-measured deformation associated with the 2004–2006 dome-building eruption of Mount St. Helens, Washington, in *A Volcano Rekindled: The Renewed Eruption of Mount St. Helens., 2004–2006*, *U.S. Geol. Surv. Prof. Pap.*, vol. 1750, edited by D. R. Sherrod, W. E. Scott, and P. H. Stauffer, chap. 15, pp. 301–333, U.S. Geol. Surv., Reston, Va.

Liuzzo, M., S. Gurrieri, G. Giudice, and G. Giuffrida (2013), Ten years of soil CO_2 continuous monitoring on Mt. Etna: Exploring the relationship between processes of soil degassing and volcanic activity, *Geochem. Geophys. Geosyst.*, *14*, 2886–2899, doi:10.1002/ggge.20196.

McNutt, S. R., H. Rymer, and J. Stix (2000), Synthesis of volcano monitoring, in *Encyclopedia of Volcanoes*, edited by H. Sigurdsson et al., pp. 1167–1185, Academic Press, San Diego, Calif.

Mogi, K. (1958), Relations between the eruptions of various volcanoes and the deformations of the ground surfaces around them, *Bull. Earthquake Res. Inst., Univ. Tokyo*, *36*, 99–134.

Moran, S. C., S. D. Malone, A. I. Qamar, W. A. Thelen, A. K. Wright, and J. Caplan-Auerbach (2008), Seismicity associated with the renewed dome-building eruption of Mount St. Helens 2004–2005, in *A Volcano Rekindled: The Renewed Eruption of Mount St. Helens, 2004–2006*, *U.S. Geol. Surv. Prof. Pap.*, vol. 1750, edited by D. R. Sherrod, W. E. Scott, and P. H. Stauffer, pp. 27–54, U.S. Geol. Surv.

Neidell, N., and M. T. Taner (1971), Semblance and other coherency measures for multichannel data, *Geophysics*, *36*, 482–497.

Palano, M., G. Puglisi, and S. Gresta (2008), Ground deformation patterns at Mt. Etna from 1993 to 2000 from joint use of InSAR and GPS techniques, *J. Volcanol. Geotherm. Res.*, *169*(3–4), 99–120, doi:10.1016/j.jvolgeores.2007.08.014.

Palano, M., M. Rossi, F. Cannavò, V. Bruno, M. Aloisi, D. Pellegrino, M. Pulvirenti, G. Siligato, and M. Mattia (2010), Etn@ref, a geodetic reference frame for Mt. Etna GPS networks, *Ann. Geophys.*, *53*(4), 48–79, doi:10.4401/af-4879.

Patanè, D., G. Di Grazia, A. Cannata, P. Montalto, and E. Boschi (2008), The shallow magma pathway geometry at Mt. Etna volcano, *Geochem. Geophys. Geosyst.*, *9*, Q12021, doi:10.1029/2008GC002131.

Patanè, D., et al. (2013), Insights into magma and fluid transfer at Mount Etna by a multiparametric approach: A model of the events leading to the 2011 eruptive cycle, *J. Geophys. Res. Solid Earth*, *118*, 3519–3539, doi:10.1002/jgrb.50248.

Rivet, D., F. Brenguier, D. Clarke, N. M. Shapiro, and A. Peltier (2014), Long-term dynamics of Piton de la Fournaise volcano from 13 years of seismic velocity change measurements and GPS observations, *J. Geophys. Res. Solid Earth*, *119*, 7654–7666, doi:10.1002/2014JB011307.

Rothery, D. A., M. Coltelli, D. Pirie, and M. J. Wooster (2001), Documenting surface magmatic activity at Mount Etna using ATSR remote sensing, *Bull. Volcanol.*, *63*, 387–397.

Scarpa, R., and P. Gasparini (1996), A review of volcano geophysics and volcano-monitoring methods, in *Monitoring and Mitigation of Volcano Hazards*, edited by R. Scarpa and R. I. Tilling, pp. 3–22, Springer, Berlin.

Sciotto, M., A. Cannata, E. Privitera, S. Gresta, and G. Di Grazia (2011), Seismo-acoustic investigations of paroxysmal activity at Mt. Etna volcano: New insights into 16 November 2006, *J. Geophys. Res.*, *116*, B09301, doi:10.1029/2010JB008138.

Spampinato, L., M. Sciotto, A. Cannata, F. Cannavò, A. La Spina, M. Palano, G. G. Salerno, E. Privitera, and T. Caltabiano (2015), Multiparametric study of the February–April 2013 paroxysmal phase of Mt. Etna New South-East crater, *Geochem. Geophys. Geosyst.*, *16*, 1932–1949, doi:10.1002/2015GC005795.

Spina, L., A. Cannata, E. Privitera, S. Vergniolle, C. Ferlito, S. Gresta, P. Montalto, and M. Sciotto (2014), Insights into Mt. Etna's shallow plumbing system from the analysis of infrasound signals, August 2007–December 2009, *Pure Appl. Geophys.*, *172*, 473–490, doi:10.1007/s00024-014-0884-x.

Takeo, M., Y. Aoki, T. Ohminato, and M. Yamamoto (2006), Magma supply path beneath Mt. Asama volcano, Japan, *Geophys. Res. Lett.*, *33*, L15310, doi:10.1029/2006GL026247.

Tarasewicz, J., R. S. White, A. W. Woods, B. Brandsdóttir, and M. T. Gudmundsson (2012), Magma mobilization by downward-propagating decompression of the Eyjafjallajökull volcanic plumbing system, *Geophys. Res. Lett.*, *39*, L19309, doi:10.1029/2012GL053518.

Tiampo, K. F., J. B. Rundle, J. Fernandez, and J. O. Langbein (2000), Spherical and ellipsoidal volcanic sources at Long Valley caldera, California, using a genetic algorithm inversion technique, *J. Volcanol. Geotherm. Res.*, *102*(3), 189–206.

Varley, N., R. Arámbula-Mendoza, G. Reyes-Dávila, J. Stevenson, and J. Harwood (2010), Long-period seismicity during magma movement at Volcán de Colima, *Bull. Volcanol.*, *72*, 1093–1107, doi:10.1007/s00445-010-0390-7.

Viccaro, M., I. Garozzo, A. Cannata, G. Di Grazia, and S. Gresta (2014), Gas burst vs. gas-rich magma recharge: A multidisciplinary study to reveal factors controlling duration of the recent paroxysmal eruptions at Mt. Etna, *J. Volcanol. Geotherm. Res.*, *278–279*, 1–13.

Williams, C. A., and G. Wadge (2000), An accurate and efficient method for including the effects of topography in three-dimensional elastic models of ground deformation with applications to radar interferometry, *J. Geophys. Res.*, *105*(B4), 8103–8120, doi:10.1029/1999JB900307.

Yang, X. M., P. M. Davis, and J. H. Dieterich (1988), Deformation from inflation of a dipping finite prolate spheroid in an elastic half-space as a model for volcanic stressing, *J. Geophys. Res.*, *93*(B5), 4249–4257, doi:10.1029/JB093iB05p04249.